# Research and Design of Misalignment-Tolerant LCC–LCC Compensated IPT System With Constant-Current and Constant-Voltage Output

Jingang Li, Xuze Zhang, and Xiangqian Tong, *Member, IEEE*

***Abstract*—It is well known that loads of inductive power transfer systems are often energy storage devices. The major benefit of an LCC–LCC compensation topology is that without the additional compensation elements and control methods, the load-independent constant current (CC) and constant voltage (CV) outputs, required by energy storage load, can be achieved at different resonant frequencies. However, the misalignment between two coils at the transmitting and receiving sides is inevitable and can lead to the variation of the resonant frequency in CC or CV output. Therefore, a unique design approach to the LCC–LCC compensation topology is proposed in this article. With the presented method, the resonant frequency, at which load-independent output characteristics can be also implemented, is constant and unaffected by the coupling coefficient, whether in CC mode or CV mode. Furthermore, the transmission gain, which is only impacted by the coupling coefficient, can be conveniently modified by the conventional phase shift control in two modes. Finally, a 120-W prototype is designed to verify the validity of the theoretical analysis. The output current and output voltage fluctuate by only 2.4% and 1.0% in the coupling coefficient range from 0.23 to 0.3 and the large load range, according to experimental results.**

***Index Terms*—Constant current (CC)/constant voltage (CV), LCC–LCC compensated topology, load independence, misalignment tolerance.**

## I. Introduction

IN CONTRAST to the traditional physical contact charging method, the inductive power transfer (IPT) technology caters to better convenience, intelligence, and stronger environmental adaptability in many applications, such as implantable medical devices, light rail vehicles, and electric vehicles [1], [2], [3], [4], [5], [6]. The IPT technology is adopted in these applications to charge energy storage devices, such as lithium-ion batteries, and to increase the life and cycle duration of these devices, so the initial constant current (CC) output procedure and the subsequent constant voltage (CV) output procedure must be implemented. However, the variation of the coupling coefficient, i.e., the misalignment between two coils at the transmitting and receiving sides, has a serious impact on the system performance. Consequently, it is not a trivial design task to implement two output modes over the variations of the misalignment between two coils at the transmitting and receiving sides and the load.

Solutions to compensate for the variation of the coupling coefficient are proposed. By optimizing the design of the coupler, a relatively uniform magnetic field distribution can be obtained for the constant output power [7], [8], [9], [10]. Complex control strategies, such as multifrequency phase-shifted control [11], are employed to enhance the misalignment-tolerant characteristic. In addition, various hybrid compensation topologies have been adopted to achieve constant transfer power with misalignment in recent years. A novel series–hybrid topology is proposed to achieve the target power transfer from −80 mm to +120 mm 1-D lateral misalignment [12]. Capacitors are required to compensate the IPT system, whereas inductors are required to tune the capacitive power transfer system. Therefore, the hybrid inductive and capacitive wireless power transfer system is proposed to transfer the target power [13], [14]. However, none of the above methods involves CC or CV charging.

Consequently, the compensation topology with the misalignment-tolerant CV or CC is paid more and more attention. The hybrid coupler and hybrid compensation topology are adopted to improve the misalignment-tolerant ability for CV or CC output [15], [16]. Based on the characteristics of the series/series–parallel compensation topology, the hybrid control with the dynamic compensation and parametric design method is proposed to implement CC or CV output over the wide misalignment and load variation [17], [18], [19]. Likewise, a novel design method of the T-series topology with misalignment tolerance is proposed to achieve CC output [20]. Nevertheless, only a single CC or CV output can be implemented over the wide range of the load and misalignment in these considerable efforts. To implement both CC and CV functions, an increasing number of efforts are accomplished. A variable inductor is integrated into a series–series network to compensate for the variation of the coupling coefficient and load [21]. However, the implementation of the variable inductor requires a complex control strategy, which increases the complexity of the control system and does not facilitate the design of the control system. In [22], to improve the misalignment tolerance

Manuscript received 12 March 2022; revised 26 May 2022 and 18 July 2022; accepted 16 August 2022. Date of publication 24 August 2022; date of current version 10 October 2022. Recommended for publication by Associate Editor A. Kuperman. *(Corresponding author: Xuze Zhang.)*

The authors are with the School of Electrical Engineering, Xi'an University of Technology, Xi'an 710048, China (e-mail: 18351055@qq.com; 646652385@qq.com; xqtong@xaut.edu.cn).

Color versions of one or more figures in this article are available at https://doi.org/10.1109/TPEL.2022.3201124.

Digital Object Identifier 10.1109/TPEL.2022.3201124

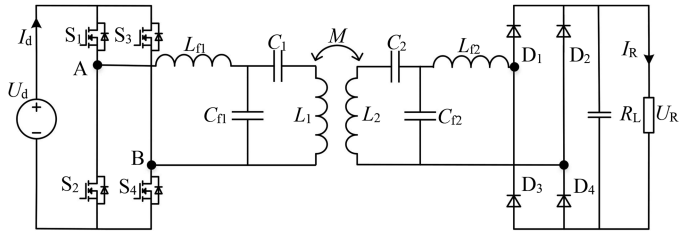


Fig. 1. LCC–LCC compensated IPT converter.

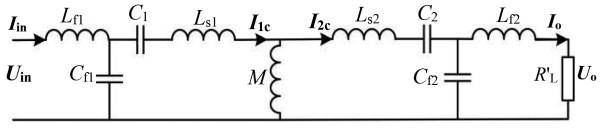


Fig. 2. Leakage inductance equivalent model of the LCC–LCC compensation topology.

of inductor–capacitor–capacitor compensation topology, the dc–dc converter and switch-controlled capacitor are employed. To implement two output modes, a hybrid reconfigurable compensation network is adopted in [23]. But the transition of two modes depends on two bidirectional power switches, which are dissipative components, and the hybrid topology has only unidirectional misalignment tolerance.

Owing to several benefits, such as more resonant frequencies and high degree of design freedom, the LCC–LCC topology has been widely researched [24], [25], [26], [27], [28], [29], [30], [31]. The work in [24] and [25] is that the capacitance matrix and auxiliary coil are adopted to compensate for the misalignment to implement CC output. However, these strategies require additional compensation elements, leading to an increase in the system size. Two auxiliary switches are employed to change the output characteristics of the LCC–LCC compensation topology for implementing two modes [26], [27]. The penalty is that additional switches and the associated driver circuitry result in the reduction of efficiency. To eliminate additional components and switches, several design methods based on several equivalence models are proposed and load-independent CC and CV outputs can be implemented at different resonant frequencies [28], [29], [30], [31]. However, these resonant frequencies vary with the misalignment. To track the resonant frequency, the unified bidirectional tracking algorithm in [32] and [33] should be analyzed and adopted.

For tackling the aforementioned concerns, a unique design approach of the LCC–LCC compensation circuit is given to implement two different output modes, over a wide load range and misalignment between two coils at the transmitting and receiving sides. The proposed method offers the following advantages over the previous method [24], [25], [26], [27], [28], [29], [30], [31].

1) Without any auxiliary coil, auxiliary compensation components, or auxiliary switch, the proposed IPT charger is able to implement both two modes, which provides efficiency, cost, and volume advantages.
2) The resonant frequencies in two modes are not only independent of the coupling coefficient but also unaffected by the load. Consequently, the system operates at a constant frequency for CC or CV mode, which helps to assure the IPT charger's reliability.
3) In the absence of any complicated control technique, the conventional phase shift control is applied to compensate for variations in output current or voltage, caused by the misalignment between the coils at the primary and secondary sides. This means that the complexity of the control system is greatly reduced.

Additionally, the rest of this article is composed as follows. The misalignment-tolerant characteristics of resonant frequencies in two modes are analyzed in Section II. Section III presents the design procedure of the presented method. Section IV reveals the simulation and experimental results. Finally, Section V concludes this article.

## II. Analysis of LCC–LCC Compensation Topology

Fig. 1 depicts the LCC–LCC compensation network [24], [25], [26], [27], [28], [29], [30], [31]. $L_1$, $L_2$, and $M$ denote the self-inductance of two coils at the transmitter and receiver and mutual inductance, respectively. The LCC circuit at the transmitting side consists of $L_{f1}$, $C_{f1}$, and $C_1$, and that at the receiving side consists of $L_{f2}$, $C_{f2}$, and $C_2$. $R_L$ depicts the load. $U_R$ and $I_R$ depict the output voltage and output current of the IPT converter, respectively. The inverter, employed to drive the input dc voltage $U_d$, is made up of four MOSFETs $S_{1,2,3,4}$. The rectifier consists of four Schottky diodes.

As depicted in Fig. 2, the LCC–LCC compensation circuit can be equated to the leakage equivalent model [26]. $L_{s1}$ and $L_{s2}$ are the leakage inductance of two coils at the transmitting and receiving sides. $\boldsymbol{U_{in}}, \boldsymbol{I_{in}}, \boldsymbol{U_o}$, and $\boldsymbol{I_o}$ are the phasors of the input voltage, input current, output voltage and output current, whereas $\boldsymbol{I_1}$ and $\boldsymbol{I_2}$ represent vectors of the current flowing through $L_{s1}$ and $L_{s2}$. $U_{in}$, $I_{in}$, $I_1$, $I_2$, $U_o$, and $I_o$ are the root-mean-square values of corresponding variables.

The primary leakage inductance $L_{s1}$, the secondary leakage inductance $L_{s2}$, $R'_L$, and the coupling coefficient $k$ are expressed as [26]

$$L_{s1} = L_1 - M, L_{s2} = L_2 - M, k = \frac{M}{\sqrt{L_1 L_2}}, R'_L = \frac{8R_L}{\pi^2}. \tag{1}$$

### A. Misalignment-Independent Resonant Frequency in the CC Mode

Based on Kirchhoff's law, the KVL matrix equation can be obtained as

$$\begin{bmatrix} \boldsymbol{U}_{in} \\ 0 \\ 0 \\ 0 \end{bmatrix} = \begin{bmatrix} jZ_{f1} & -\frac{1}{j\omega C_{f1}} & 0 & 0 \\ -\frac{1}{j\omega C_{f1}} & jZ_1 & -j\omega M & 0 \\ 0 & -j\omega M & jZ_2 & -\frac{1}{j\omega C_{f2}} \\ 0 & 0 & -\frac{1}{j\omega C_{f2}} & jZ_{f2} + R'_L \end{bmatrix} \begin{bmatrix} \boldsymbol{I_{in}} \\ \boldsymbol{I_{1c}} \\ \boldsymbol{I_{2c}} \\ \boldsymbol{I_o} \end{bmatrix} \tag{2}$$

where $\boldsymbol{I_{1c}}$ and $\boldsymbol{I_{2c}}$ represent $\boldsymbol{I_1}$ and $\boldsymbol{I_2}$ in the CC mode. $Z_{\mathrm{f1}}, Z_1$, $Z_2$, and $Z_{\mathrm{f2}}$ can be written as

$$\begin{cases} Z_{\mathrm{f1}} = \omega L_{\mathrm{f1}} - \frac{1}{\omega C_{\mathrm{f1}}} \\ Z_{\mathrm{f2}} = \omega L_{\mathrm{f2}} - \frac{1}{\omega C_{\mathrm{f2}}} \\ Z_1 = \omega M + \omega L_{\mathrm{s1}} - \frac{1}{\omega C_{\mathrm{f1}}} - \frac{1}{\omega C_1} \\ Z_2 = \omega M + \omega L_{\mathrm{s2}} - \frac{1}{\omega C_{\mathrm{f2}}} - \frac{1}{\omega C_2} \end{cases}. \tag{3}$$

It is easily derived from (2) that the ratio of the input voltage $\boldsymbol{U_{in}}$ to the output current $\boldsymbol{I_o}$ is expressed as

$$\begin{aligned} \frac{\boldsymbol{U}_{in}}{\boldsymbol{I}_{\mathrm{o}}} = \frac{C_{\mathrm{f2}}\left(jZ_{\mathrm{f2}}+R'_{\mathrm{L}}\right)}{M}\left(\omega C_{\mathrm{f1}} Z_1 Z_2 Z_{\mathrm{f1}}\right. \\ \left. -\omega^3 M^2 C_{\mathrm{f1}} Z_{\mathrm{f1}} - \frac{Z_2}{\omega C_{\mathrm{f1}}}\right) \\ + \frac{j}{\omega M C_{\mathrm{f2}}}\left(\frac{1}{\omega^2 C_{\mathrm{f1}}} - C_{\mathrm{f1}} Z_1 Z_{\mathrm{f1}}\right). \end{aligned} \tag{4}$$

Combining (1) and (4), if the components $L_{\mathrm{f1}}$, $C_{\mathrm{f1}}$, $C_2$, and $C_{\mathrm{f2}}$ are selected to satisfy the condition in (5), i.e., $Z_{\mathrm{f1}} = 0$ and $Z_2 = 0$, the output current $\boldsymbol{I_{o\text{-}c}}$ is unaffected by the equivalent load and can be expressed as (6). It can be concluded from (5) that the resonant angle frequency $\omega_{\mathrm{c}}$ maintains a constant value and cannot be affected by the coupling coefficient.

$$\omega_{\mathrm{c}}^2 = \frac{1}{L_{\mathrm{f1}} C_{\mathrm{f1}}} = \frac{1}{L_2}\left(\frac{1}{C_{\mathrm{f2}}} + \frac{1}{C_2}\right) \tag{5}$$

$$\boldsymbol{I_{o-c}} = -j\omega_{\mathrm{c}}^3 k\sqrt{L_1 L_2} C_{\mathrm{f1}} C_{\mathrm{f2}} \boldsymbol{U_{in}}. \tag{6}$$

In practice, the capacitor decreases as the charging time increases or the temperature rises. According to (4) and (5), the tolerance of the compensation components $C_1$ and $L_{\mathrm{f2}}$ cannot affect the output current, whereas the condition of load-independent CC output cannot be satisfied if components $L_{\mathrm{f1}}$, $C_{\mathrm{f1}}$, $C_2$, and $C_{\mathrm{f2}}$ vary. Thus, it is necessary to analyze the tolerance of components.

Based on (3)–(5), if $L_{\mathrm{f1}}$, $C_{\mathrm{f1}}$, $C_2$, or $C_{\mathrm{f2}}$ varies, the output current $\boldsymbol{I_{o\text{-}Cf1}}, \boldsymbol{I_{o\text{-}Lf1}}, \boldsymbol{I_{o\text{-}C2}}$, and $\boldsymbol{I_{o\text{-}Cf2}}$ can be further deduced as

$$\boldsymbol{I_{o-Cf1}} = \frac{\frac{\boldsymbol{U_{in}}\omega_{\mathrm{c}}^3 M C_{\mathrm{f2}} C_{\mathrm{f1}}}{\Delta C_{\mathrm{f1}}}}{\frac{C_{\mathrm{f1}}}{\Delta C_{\mathrm{f1}}(C_{\mathrm{f1}}-\Delta C_{\mathrm{f1}})} - \omega_{\mathrm{c}}^5 M^2 C_{\mathrm{f2}}^2 Z_{\mathrm{f2}} - \omega_{\mathrm{c}} Z_1 + j\omega_{\mathrm{c}}^5 M^2 C_{\mathrm{f2}}^2 R'_{\mathrm{L}}} \tag{7}$$

$$\boldsymbol{I_{o-Lf1}} = \frac{\frac{\boldsymbol{U_{in}}}{\Delta L_{\mathrm{f1}}}}{\frac{M C_{\mathrm{f2}} R'_{\mathrm{L}}}{L_{\mathrm{f1}}^2 C_{\mathrm{f1}}} + j\left(\frac{M C_{\mathrm{f2}} Z_{\mathrm{f2}}}{L_{\mathrm{f1}}^2 C_{\mathrm{f1}}} + \frac{L_{\mathrm{f1}}}{\omega_{\mathrm{c}} \Delta L_{\mathrm{f1}} M C_{\mathrm{f2}}} + \frac{C_{\mathrm{f1}} Z_1}{M C_{\mathrm{f2}}}\right)} \tag{8}$$

$$\boldsymbol{I_{o-C2}} = \frac{\boldsymbol{U_{in}}\omega_{\mathrm{c}}^3 C_{\mathrm{f1}} M C_{\mathrm{f2}} C_2 (C_2 - \Delta C_2)}{C_2(C_2-\Delta C_2) - \omega_{\mathrm{c}} \Delta C_2 C_{\mathrm{f2}}^2 (Z_{\mathrm{f2}} - jR'_{\mathrm{L}})} \tag{9}$$

$$\boldsymbol{I_{o-Cf2}} = \frac{\boldsymbol{U_{in}}\omega_{\mathrm{c}}^3 C_{\mathrm{f1}} M C_{\mathrm{f2}} (C_{\mathrm{f2}} - \Delta C_{\mathrm{f2}})}{C_{\mathrm{f2}} - \omega_{\mathrm{c}} \Delta C_{\mathrm{f2}} (C_{\mathrm{f2}} - \Delta C_{\mathrm{f2}})(Z_{\mathrm{f2}} - jR'_{\mathrm{L}})} \tag{10}$$

where $\Delta L_{\mathrm{f1}}$, $\Delta C_{\mathrm{f1}}$, $\Delta C_2$, and $\Delta C_{\mathrm{f2}}$ express the tolerance of corresponding components.

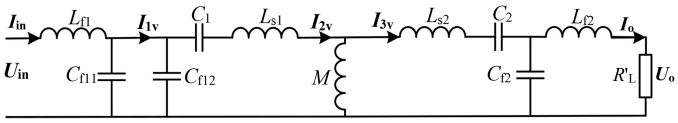


Fig. 3. Leakage inductance equivalent model of LCC–LCC compensation topology for the CV mode.

It is easily derived from (7) to (10) that whether $L_{\mathrm{f1}}$, $C_{\mathrm{f1}}$, $C_2$, or $C_{\mathrm{f2}}$ varies, the characteristic of load-independent CC output is influenced and output currents $\boldsymbol{I_{o\text{-}Cf1}}, \boldsymbol{I_{o\text{-}Lf1}}, \boldsymbol{I_{o\text{-}C2}}$, and $\boldsymbol{I_{o\text{-}Cf2}}$ decreases as the load increases.

From (2), (5), and (6), currents $\boldsymbol{I_{1c}}$ and $\boldsymbol{I_{2c}}$ of the resonant network are expressed as follows in the CC mode:

$$\begin{cases} \boldsymbol{I_{1c}} = \frac{\boldsymbol{U_{in}}}{\omega_{\mathrm{c}} L_{\mathrm{f1}}}\left[Z_2 \omega_{\mathrm{c}}^2 C_{\mathrm{f2}}^2 R'_{\mathrm{L}} + j\left(Z_2 \omega_{\mathrm{c}}^2 C_{\mathrm{f2}}^2 Z_{\mathrm{f2}} - 1\right)\right] \\ \boldsymbol{I_{2c}} = \frac{\boldsymbol{U_{in}}\omega_{\mathrm{c}}^2 C_{\mathrm{f2}}^2 M (R'_{\mathrm{L}} + jZ_{\mathrm{f2}})}{L_{\mathrm{f1}}} \end{cases}. \tag{11}$$

### *B. Misalignment-Independent Resonant Frequency in the CV Mode*

It is easily deduced from (4) that the ratio of the input voltage $\boldsymbol{U_{in}}$ to the output voltage $\boldsymbol{U_o}$ can be expressed in (12). It is clear from (12) that the resonant frequency, at which the load-independent output voltage is implemented, consistently varies with the mutual inductance.

$$\begin{aligned} \frac{\boldsymbol{U_{in}}}{\boldsymbol{U}_{\mathrm{o}}} = \frac{jC_{\mathrm{f2}} Z_{\mathrm{f2}}}{M R'_{\mathrm{L}}}\left(\omega C_{\mathrm{f1}} Z_1 Z_2 Z_{\mathrm{f1}} - \omega^3 M^2 C_{\mathrm{f1}} Z_{\mathrm{f1}} - \frac{Z_2}{\omega C_{\mathrm{f1}}}\right) \\ + \frac{j}{M R'_{\mathrm{L}} \omega C_{\mathrm{f2}}}\left(\frac{1}{\omega^2 C_{\mathrm{f1}}} - C_{\mathrm{f1}} Z_1 Z_{\mathrm{f1}}\right) \\ + \frac{C_{\mathrm{f2}}}{M}\left(\omega C_{\mathrm{f1}} Z_1 Z_2 Z_{\mathrm{f1}} - \omega^3 M^2 C_{\mathrm{f1}} Z_{\mathrm{f1}} - \frac{Z_2}{\omega C_{\mathrm{f1}}}\right). \end{aligned} \tag{12}$$

Therefore, to obtain the constant resonant frequency irrelevant to the misalignment, Fig. 2 can be equated to Fig. 3, where $C_{\mathrm{f11}}$ and $C_{\mathrm{f12}}$ can be expressed as

$$C_{\mathrm{f11}} + C_{\mathrm{f12}} = C_{\mathrm{f1}}. \tag{13}$$

Similarly, the KVL matrix equation of this model can be obtained as

$$\begin{bmatrix} \boldsymbol{U_{in}} \\ 0 \\ 0 \\ 0 \\ 0 \end{bmatrix} = \begin{bmatrix} jZ_{\mathrm{f1-v}} & -\frac{1}{j\omega C_{\mathrm{f11}}} & 0 & 0 & 0 \\ -\frac{1}{j\omega C_{\mathrm{f11}}} & jZ_{\mathrm{s}} & -\frac{1}{j\omega C_{\mathrm{f12}}} & 0 & 0 \\ 0 & -\frac{1}{j\omega C_{\mathrm{f12}}} & jZ_{\mathrm{1-v}} & -j\omega M & 0 \\ 0 & 0 & -j\omega M & jZ_2 & -\frac{1}{j\omega C_{\mathrm{f2}}} \\ 0 & 0 & 0 & -\frac{1}{j\omega C_{\mathrm{f2}}} & jZ_{\mathrm{f2}} + R'_{\mathrm{L}} \end{bmatrix} \begin{bmatrix} \boldsymbol{I_{in}} \\ \boldsymbol{I_{1v}} \\ \boldsymbol{I_{2v}} \\ \boldsymbol{I_{3v}} \\ \boldsymbol{I_o} \end{bmatrix} \tag{14}$$

where $Z_{\text{f1-v}}$, $Z_{\text{1-v}}$, and $Z_{\text{s}}$ can be written as

$$\begin{cases} Z_{\text{f1-v}} = \omega L_{\text{f1}} - \frac{1}{\omega C_{\text{f11}}} \\ Z_{\text{s}} = -\frac{1}{\omega C_{\text{f11}}} - \frac{1}{\omega C_{\text{f12}}} \\ Z_{\text{1-v}} = \omega M + \omega L_{\text{s1}} - \frac{1}{\omega C_{\text{f12}}} - \frac{1}{\omega C_1} \end{cases}. \tag{15}$$

From (14), the ratio of the input voltage $\boldsymbol{U_{in}}$ to the output voltage $\boldsymbol{U_o}$ is represented in

$$\frac{\boldsymbol{U_{in}}}{\boldsymbol{U_o}} = -\omega C_{\text{f2}} A - \frac{j}{R'_{\text{L}}}\left(\omega C_{\text{f2}} Z_{\text{f2}} A + \frac{B}{\omega^2 M C_{\text{f12}}}\right) \tag{16}$$

where

$$A = \frac{Z_2 Z_{\text{f1-v}}}{\omega^2 M C_{\text{f12}}} + \frac{\omega M C_{\text{f12}}}{C_{\text{f11}}} + \frac{Z_2 Z_{\text{1-v}} C_{\text{f12}}}{\omega M C_{\text{f11}}} - \frac{\omega C_{\text{f11}} Z_2 Z_{\text{1-v}} Z_{\text{s}} Z_{\text{f1-v}}}{M} - \omega^3 C_{\text{f11}} C_{\text{f12}} M Z_{\text{s}} Z_{\text{f1-v}} \tag{17}$$

$$B = \frac{C_{\text{f12}} Z_{\text{1-v}}}{C_{\text{f11}}} + \frac{Z_{\text{f1-v}}}{\omega C_{\text{f12}}} - \omega^2 C_{\text{f11}} C_{\text{f12}} Z_{\text{1-v}} Z_{\text{s}} Z_{\text{f1-v}}. \tag{18}$$

Obviously, it can be observed from (16) that if the condition in (19) is satisfied, i.e., $Z_{\text{f1-v}}$, $Z_{\text{1-v}}$, and $Z_{\text{f2}}$ are equal to zero, the output voltage $\boldsymbol{U_o}$ can be expressed as (20). It can be observed from (19) that the resonant frequency is constant regardless of the coupling coefficient.

$$\omega_{\text{v}}^2 = \frac{1}{L_{\text{f1}} C_{\text{f11}}} = \frac{1}{L_1}\left(\frac{1}{C_{\text{f12}}} + \frac{1}{C_1}\right) = \frac{1}{L_{\text{f2}} C_{\text{f2}}} \tag{19}$$

$$\boldsymbol{U_{o-v}} = \frac{-\boldsymbol{U_{in}}}{\omega_{\text{v}}^4 C_{\text{f2}} k \sqrt{L_1 L_2} L_{\text{f1}} C_{\text{f12}}}. \tag{20}$$

The same as the CC mode, according to (16) and (19), the tolerance of the compensation components $C_2$ cannot affect the output current, whereas the condition of load-independent CV output cannot be satisfied if components $L_{\text{f1}}$, $C_{\text{f1}}$, $C_2$, $L_{\text{f2}}$, or $C_{\text{f2}}$ varies.

Based on (16) and (19), the tolerance of the inductor $L_{\text{f1}}$ can affect the condition in $Z_{\text{f1-v}} = 0$, whereas if capacitor $C_{\text{f1}}$ varies, since $C_{\text{f1}}$ is composed of $C_{\text{f11}}$ and $C_{\text{f12}}$, the tolerance of $C_{\text{f1}}$ cannot affect the resonant condition in $Z_{\text{f1-v}} = 0$, but affect the resonant condition in $Z_{\text{1-v}} = 0$. The same as $C_{\text{f1}}$, the tolerance of $C_1$ can also influence the resonant condition in $Z_{\text{1-v}} = 0$. If $C_{\text{f2}}$ and $L_{\text{f2}}$ vary, the resonant condition in $Z_{\text{f2}} = 0$ cannot be satisfied. Therefore, the output voltage $\boldsymbol{U_{o\text{-}Lf1}}$, $\boldsymbol{U_{o\text{-}Cf1}}$, $\boldsymbol{U_{o\text{-}C1}}$, $\boldsymbol{U_{o\text{-}Cf2}}$, and $\boldsymbol{U_{o\text{-}Lf2}}$ can be further deduced as

$$\boldsymbol{U_{o-Lf1}} = \frac{\boldsymbol{U_{in}}}{\frac{\omega_{\text{v}} C_{\text{f2}}}{C_{\text{f12}}}\left(\frac{M Z_{\text{s}} \Delta L_{\text{f1}}}{L_{\text{f1}}^2 C_{\text{f11}}} - \frac{Z_2 \Delta L_{\text{f1}}}{\omega_{\text{v}} M C_{\text{f2}}^2} - \frac{\omega_{\text{v}} M}{C_{\text{f11}}}\right) - \frac{j \Delta L_{\text{f1}}}{\omega_{\text{v}}^2 M C_{\text{f2}}^2 R'_{\text{L}}}} \tag{21}$$

$$\boldsymbol{U_{o-Cf1}} = \frac{-\boldsymbol{U_{in}} C_{\text{f11}}}{\omega_{\text{v}}^2 C_{\text{f2}} M\left(C_{\text{f12}} - \Delta C_{\text{f1}}\right)\left(1 + \frac{Z_2 \Delta Z_{\text{1-v-Cf1}}}{\omega_{\text{v}}^2 M^2}\right) + \frac{j \Delta Z_{\text{1-v-Cf1}} C_{\text{f2}}}{\omega_{\text{v}}^2 M R'_{\text{L}}}} \tag{22}$$

$$\boldsymbol{U_{o-C1}} = \frac{-\boldsymbol{U_{in}} C_{\text{f11}}}{\omega_{\text{v}}^2 C_{\text{f2}} M C_{\text{f12}}\left(1 + \frac{Z_2 \Delta Z_{\text{1-v-C1}}}{\omega_{\text{v}}^2 M^2}\right) + \frac{j \Delta Z_{\text{1-v-C1}} C_{\text{f2}}}{\omega_{\text{v}}^2 M R'_{\text{L}}}} \tag{23}$$

$$\boldsymbol{U_{o-Cf2}} = \frac{-\boldsymbol{U_{in}} C_{\text{f11}}}{\omega_{\text{v}}^2 C_{\text{f12}} M\left(C_{\text{f2}} - \Delta C_{\text{f2}}\right) + j \frac{\omega_{\text{v}} C_{\text{f12}} M \Delta C_{\text{f2}}}{R'_{\text{L}} C_{\text{f2}}}} \tag{24}$$

$$\boldsymbol{U_{o-Lf2}} = \frac{-\boldsymbol{U_{in}} C_{\text{f11}}}{\omega_{\text{v}}^2 C_{\text{f12}} M C_{\text{f2}} + j \frac{\omega_{\text{v}}^3 C_{\text{f2}} C_{\text{f12}} M \Delta L_{\text{f2}}}{R'_{\text{L}}}} \tag{25}$$

where $\Delta Z_{\text{1-v-Cf1}}$, $\Delta Z_{\text{1-v-C1}}$, $\Delta L_{\text{f1}}$, $\Delta C_{\text{f1}}$, $\Delta C_1$, $\Delta C_{\text{f2}}$, and $\Delta L_{\text{f2}}$ express the tolerance of corresponding components

$$\Delta Z_{\text{1-v-Cf1}} = \frac{\Delta C_{\text{f1}}}{\omega_{\text{v}} C_{\text{f12}}\left(C_{\text{f12}} - \Delta C_{\text{f1}}\right)} \tag{26}$$

$$\Delta Z_{\text{1-v-C1}} = \frac{\Delta C_1}{\omega_{\text{v}} C_1\left(C_1 - \Delta C_1\right)}. \tag{27}$$

From (21) to (25), compared to CC mode, the output voltage increases with the load, whether component $L_{\text{f1}}$, $C_{\text{f1}}$, $C_2$, $L_{\text{f2}}$, or $C_{\text{f2}}$ varies.

From (14), (19), and (20), currents $\boldsymbol{I_{1v}}$, $\boldsymbol{I_{2v}}$, and $\boldsymbol{I_{3v}}$ of the resonant network are represented in the following equation in the CV mode:

$$\begin{cases} \boldsymbol{I_{1v}} = \frac{\boldsymbol{U_{in}}}{\omega_{\text{v}}^2 L_{\text{f1}} R'_{\text{L}}}\left[\left(1 - \frac{Z_{\text{1-v}} Z_2}{\omega_{\text{v}}^2 M^2}\right)\left(Z_{\text{f2}} - j R'_{\text{L}}\right) + \frac{j Z_{\text{1-v}} L_{\text{f2}}}{\omega_{\text{v}}^2 M^2 C_{\text{f2}}}\right] \\ \boldsymbol{I_{2v}} = \frac{\boldsymbol{U_{in}}}{\omega_{\text{v}}^4 M^2 L_{\text{f1}} C_{\text{f12}} R'_{\text{L}}}\left(Z_2 Z_{\text{f2}} - \frac{L_{\text{f2}}}{C_{\text{f2}}} - j Z_2 R'_{\text{L}}\right) \\ \boldsymbol{I_{3v}} = \frac{\boldsymbol{U_{in}}}{\omega_{\text{v}}^3 M L_{\text{f1}} C_{\text{f12}} R'_{\text{L}}}\left(Z_{\text{f2}} - j R'_{\text{L}}\right) \end{cases}. \tag{28}$$

### C. CC Output and CV Output Under the Misalignment

It is clear from (6) and (20) that the output current and output voltage are independent of the equivalent load $R'_{\text{L}}$, but can be seriously affected by the coupling coefficient, i.e., the output current is a proportional function of the coupling coefficient in the CC mode and the output voltage is an inverse function of the coupling coefficient in the CV mode. In addition, the tolerance of compensation components can also lead to variations in the output current and output voltage. Therefore, conventional phase shift control is employed to maintain the constant transmission gain in two output modes. Fig. 4 presents the typical waveforms of drive and output signals about the phase shift control. $\boldsymbol{U_{AB}}$ can be regulated by modifying phase shift angle $\theta$. In addition, $T$ indicates the switching period. The root-mean-square values of the fundamental component $\boldsymbol{U_{AB}}$, denoted as $U_{\text{in}}$, is given as [34]

$$U_{\text{in}} = \frac{2\sqrt{2} U_{\text{d}}}{\pi} \cos\frac{\theta}{2}. \tag{29}$$

By substituting (26) into (6) and (20), the output current $I_{\text{o-c}}$ and the output voltage $U_{\text{o-v}}$ can be expressed as (30) and (31). From (30) and (31), both the CC mode and CV mode can be implemented over the misalignment by adjusting $\theta$.

$$I_{\text{o-c}} = \frac{2\sqrt{2}\omega_{\text{c}} k \sqrt{L_1 L_2} C_{\text{f2}} U_{\text{d}}}{\pi L_{\text{f1}}} \cos\frac{\theta}{2} \tag{30}$$

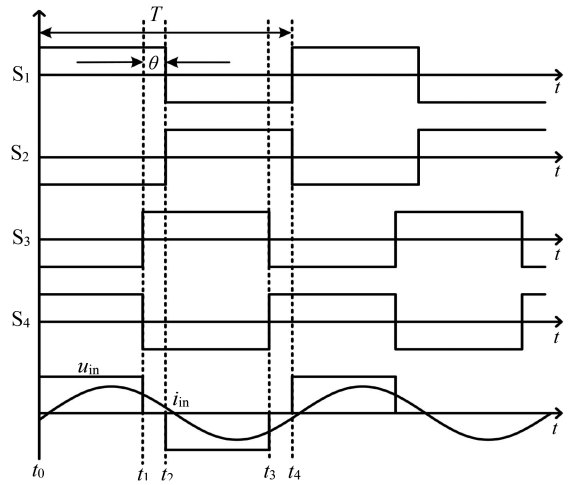


Fig. 4. Switching sequence of phase-shifted control.

$$U_{\mathrm{o-v}} = \frac{2\sqrt{2}U_{\mathrm{d}}}{\pi\omega_{\mathrm{v}}^4 C_{\mathrm{f2}} k\sqrt{L_1 L_2} L_{\mathrm{f1}} C_{\mathrm{f12}}} \cos\frac{\theta}{2}. \tag{31}$$

### D. Analysis and Reduction of Power Losses

In the proposed IPT system, the power losses are mainly composed of three parts, i.e., the losses of four rectifier diodes, the resonant circuit, and four inverter MOSFETs [34].

The forward voltage drop is primarily responsible for the power losses of the rectifier diodes. According to [34], the losses can be calculated as follows:

$$P_{\mathrm{d-loss}} = \frac{2\sqrt{2}V_{\mathrm{f}} I_{\mathrm{o}}}{\pi} + I_{\mathrm{o}}^2 r_{\mathrm{d}} \tag{32}$$

where the forward voltage drop and the ON-state resistance are expressed by $V_{\mathrm{f}}$ and $r_{\mathrm{d}}$.

Likewise, the power losses about the resonant circuit consist of the equivalent series resistances of transmitting coil, receiving coil, and compensation components, and can be expressed as [34]

$$\begin{aligned} P_{\mathrm{lc-loss}} = {} & I_{\mathrm{Lf1}}^2 r_{\mathrm{Lf1}} + I_{\mathrm{Cf1}}^2 r_{\mathrm{Cf1}} + I_{\mathrm{L1}}^2 (r_{\mathrm{C1}} + r_{\mathrm{L1}}) \\ & + I_{\mathrm{L2}}^2 (r_{\mathrm{C2}} + r_{\mathrm{L2}}) \\ & + I_{\mathrm{Lf2}}^2 r_{\mathrm{Lf2}} + I_{\mathrm{Cf2}}^2 r_{\mathrm{Cf2}} \end{aligned} \tag{33}$$

where $I_{\mathrm{Lf1}}$, $I_{\mathrm{Cf1}}$, $I_{\mathrm{L1}}$, $I_{\mathrm{L2}}$, $I_{\mathrm{Lf2}}$, and $I_{\mathrm{Cf2}}$ express the current flowing through the corresponding components and $r_{\mathrm{Lf1}}$, $r_{\mathrm{Cf1}}$, $r_{\mathrm{C1}}$, $r_{\mathrm{L1}}$, $r_{\mathrm{L2}}$, $r_{\mathrm{C2}}$, $r_{\mathrm{Lf2}}$, and $r_{\mathrm{Cf2}}$ represent equivalent resistances of the corresponding components.

The power losses of the inverter MOSFETs mainly include conduction losses and switching losses [34]. The conduction losses are derived as

$$P_{\mathrm{on-loss}} = \frac{I_{\mathrm{in}}^2 r_{\mathrm{ds}}}{\pi} (3\pi - \theta - \sin\theta) \tag{34}$$

where $r_{\mathrm{ds}}$ is the ON-state resistance of the MOSFET.

The switching loss can be calculated as

$$P_{\mathrm{switch-loss}} = -2\sqrt{2} U_{\mathrm{in}} I_{\mathrm{in}} \cos\left(\pi - \frac{\theta}{2}\right) f \left(\frac{E_{\mathrm{on}} + E_{\mathrm{off}}}{U_{\mathrm{ds}} I_{\mathrm{ds}}}\right) \tag{35}$$

where $E_{\mathrm{ON}}$, $E_{\mathrm{OFF}}$, $U_{\mathrm{ds}}$, and $I_{\mathrm{ds}}$ are the turn-ON loss, turn-OFF loss, drain–source voltage, and drain–source current of the MOSFET.

The IPT system often operates at a high frequency and the switching loss is the main power loss. As a result, it is significant to implement soft switching. For MOSFETs, zero voltage switching (ZVS) is favored over zero current soft switching. The condition in the following equation is a critical element to implement ZVS [34]:

$$I_{\mathrm{pk}} \geq \frac{2U_{\mathrm{bus}} C_{\mathrm{j}}}{t_{\mathrm{dead}}} \tag{36}$$

where $I_{\mathrm{pk}}$, $U_{\mathrm{b}}$, $C_{\mathrm{j}}$, and $t_{\mathrm{d}}$ denote the turn-OFF peak current, input voltage, parasitic capacitor, and dead time of MOSFETs, respectively.

Therefore, it is necessary to derive the input current $\boldsymbol{I_{\mathrm{in}}}$ for ZVS. Based on (2) and (14), the impedance $Z_{\mathrm{in\text{-}c}}$ and $Z_{\mathrm{in\text{-}v}}$ can be deduced as (37) and (38), respectively. From (37) and (38), if the compensation components satisfy $a_{\mathrm{c}} = 0$ or $a_{\mathrm{v}} = 0$, the input impedance angle is zero and at this point, the imaginary part increases as the coupling coefficient.

$$Z_{\mathrm{in-c}} = \frac{L_{\mathrm{f1}}}{C_{\mathrm{f1}} \left(\omega_{\mathrm{c}}^4 k^2 L_1 L_2 C_{\mathrm{f2}}^2 R'_{\mathrm{L}} - j\omega_{\mathrm{c}} a_{\mathrm{c}}\right)} \tag{37}$$

$$Z_{\mathrm{in-v}} = \frac{\omega_{\mathrm{v}}^4 C_{\mathrm{f12}}^2 k^2 L_1 L_2 L_{\mathrm{f1}} C_{\mathrm{f2}} R'_L}{C_{\mathrm{f11}} L_{\mathrm{f2}} - j C_{\mathrm{f11}} C_{\mathrm{f2}} R'_L a_{\mathrm{v}}} \tag{38}$$

where

$$\begin{aligned} a_{\mathrm{c}} = {} & \omega_{\mathrm{c}}^2 k^2 L_1 L_2 C_{\mathrm{f2}} - \omega_{\mathrm{c}}^4 k^2 L_1 L_2 C_{\mathrm{f2}}^2 L_{\mathrm{f2}} \\ & - L_1 + \frac{1}{\omega_{\mathrm{c}}^2 C_1} + \frac{1}{\omega_{\mathrm{c}}^2 C_{\mathrm{f1}}} \end{aligned} \tag{39}$$

$$a_{\mathrm{v}} = \frac{1}{\omega_{\mathrm{v}} C_{\mathrm{f2}}} + \frac{1}{\omega_{\mathrm{v}} C_2} + \omega_{\mathrm{v}}^3 C_{\mathrm{f12}}^2 k^2 L_1 L_2 \left(\frac{1}{C_{\mathrm{f11}}} + \frac{1}{C_{\mathrm{f12}}}\right) - \omega_{\mathrm{v}} L_2. \tag{40}$$

The fundamental input currents $\boldsymbol{I_{\mathrm{in\text{-}c\text{-}1st}}}$ and $\boldsymbol{I_{\mathrm{in\text{-}v\text{-}1st}}}$ of the CC mode and CV mode can be derived as

$$\boldsymbol{I_{\mathrm{in-c-1st}}} = \frac{k^2 L_1 L_2 C_{\mathrm{f2}}^2 R'_{\mathrm{L}} \boldsymbol{U_{\mathrm{in}}}}{L_{\mathrm{f1}}^3 C_{\mathrm{f1}}} - \frac{j\omega_{\mathrm{c}} C_{\mathrm{f1}} a_{\mathrm{c}} \boldsymbol{U_{\mathrm{in}}}}{L_{\mathrm{f1}}} \tag{41}$$

$$\boldsymbol{I_{\mathrm{in-v-1st}}} = \frac{L_{\mathrm{f2}}^3 C_{\mathrm{f11}} C_{\mathrm{f2}} \boldsymbol{U_{\mathrm{in}}}}{C_{\mathrm{f12}}^2 k^2 L_1 L_2 L_{\mathrm{f1}} R'_{\mathrm{L}}} - \frac{j C_{\mathrm{f11}} a_{\mathrm{v}} \boldsymbol{U_{\mathrm{in}}}}{\omega_{\mathrm{v}}^4 C_{\mathrm{f12}}^2 k^2 L_1 L_2 L_{\mathrm{f1}}}. \tag{42}$$

However, it is easy to notice from Figs. 2 and 3 that the *LC* filter network exists at the input of the compensation network in two output modes. Thus, the input current of the $(2k+1)$th harmonics in two modes can be expressed as

$$\boldsymbol{I_{\mathrm{in-c-(2k+1)th}}} \approx \frac{\boldsymbol{U_{\mathrm{in-(2k+1)th}}}}{j\,(2\mathrm{k}+1)\,\omega_{\mathrm{c}} L_{\mathrm{f1}} + \frac{1}{j(2\mathrm{k}+1)\omega_{\mathrm{c}} C_{\mathrm{f1}}}} \tag{43}$$

$$\boldsymbol{I}_{\mathbf{in-v-(2k+1)th}} \approx \frac{\boldsymbol{U}_{\mathbf{in-(2k+1)th}}}{j\left(2\mathrm{k}+1\right)\omega_{\mathrm{v}}L_{\mathrm{f1}}+\frac{1}{j(2\mathrm{k}+1)\omega_{\mathrm{v}}C_{\mathrm{f11}}}}. \quad (44)$$

It can be deduced from (43) and (44) that the high-order input currents $\boldsymbol{I}_{\mathbf{in\text{-}c\text{-}mth}}$ and $\boldsymbol{I}_{\mathbf{in\text{-}v\text{-}mth}}$ can be calculated as

$$\sum \boldsymbol{I}_{\mathbf{in-c-mth}} \approx \frac{\boldsymbol{U}_{\mathbf{in}}}{j4\omega_{\mathrm{c}}L_{\mathrm{f1}}} \quad (45)$$

$$\sum \boldsymbol{I}_{\mathbf{in-v-mth}} \approx \frac{\boldsymbol{U}_{\mathbf{in}}}{j4\omega_{\mathrm{v}}L_{\mathrm{f1}}}. \quad (46)$$

Therefore, the input currents $\boldsymbol{I}_{\mathbf{in\text{-}c}}$ and $\boldsymbol{I}_{\mathbf{in\text{-}v}}$ in both modes can be expressed as follows:

$$\boldsymbol{I}_{\mathbf{in-c}} = \boldsymbol{I}_{\mathbf{in-c-1st}} + \sum \boldsymbol{I}_{in\mathbf{-c-mth}} \quad (47)$$

$$\boldsymbol{I}_{\mathbf{in-v}} = \boldsymbol{I}_{\mathbf{in-v-1st}} + \sum \boldsymbol{I}_{\mathbf{in-v-mth}}. \quad (48)$$

If the phase shift control is adopted, the input currents $i_{\mathrm{in\text{-}c}}(\theta/2)$ and $i_{\mathrm{in\text{-}v}}(\theta/2)$ of two modes at the phase shift angle $\theta$ can be expressed as follows:

$$i_{\mathrm{in-c}}\left(\frac{\theta}{2}\right)=\frac{4U_{\mathrm{d}}k^2L_1L_2C_{\mathrm{f2}}^2R'_{\mathrm{L}}}{\pi L_{\mathrm{f1}}^3C_{\mathrm{f1}}}\cos\frac{\theta}{2}\sin\frac{\theta}{2}-\frac{4U_{\mathrm{d}}\omega_{\mathrm{c}}C_{\mathrm{f1}}a_{\mathrm{c}}}{\pi L_{\mathrm{f1}}}\cos^2\frac{\theta}{2} - \frac{U_{\mathrm{d}}}{\pi\omega_{\mathrm{c}}L_{\mathrm{f1}}}\cos^2\frac{\theta}{2} \quad (49)$$

$$i_{\mathrm{in-v}}\left(\frac{\theta}{2}\right)=\frac{4U_{\mathrm{d}}L_{\mathrm{f2}}^3C_{\mathrm{f1}}C_{\mathrm{f2}}}{\pi C_{\mathrm{f12}}^2k^2L_1L_2L_{\mathrm{f1}}R'_{\mathrm{L}}}\cos\frac{\theta}{2}\sin\frac{\theta}{2}-\frac{U_{\mathrm{d}}}{\pi\omega_{\mathrm{v}}L_{\mathrm{f1}}}\cos^2\frac{\theta}{2} - \frac{4U_{\mathrm{d}}L_{\mathrm{f2}}^2C_{\mathrm{f1}}C_{\mathrm{f2}}a_{\mathrm{v}}}{\pi C_{\mathrm{f12}}^2k^2L_1L_2L_{\mathrm{f1}}R'_{\mathrm{L}}}\cos^2\frac{\theta}{2}. \quad (50)$$

As a result, according to (36), the input currents $i_{\mathrm{in\text{-}c}}$ and $i_{\mathrm{in\text{-}v}}$ should satisfy the condition in the following equations for the implementation of ZVS:

$$-i_{\mathrm{in-c}}\left(\frac{\theta}{2}\right) \geq I_{\mathrm{pk}} \quad (51)$$

$$-i_{\mathrm{in-v}}\left(\frac{\theta}{2}\right) \geq I_{\mathrm{pk}}. \quad (52)$$

### *E. Analysis of Resonant Network RMS Current and Capacitors Voltage*

At this point, the RMS current of the resonant network should be analyzed for reasonable designing of the main switches of the proposed IPT system. According to (11), (30), and (47), the RMS current in the CC mode can be expressed as

$$\begin{aligned} I_{1\mathrm{c}} &= \frac{2\sqrt{2}U_{\mathrm{d}}}{\pi\omega_{\mathrm{c}}L_{\mathrm{f1}}}\cos\frac{\theta}{2}\sqrt{A_{1\mathrm{c}}^2+B_{1\mathrm{c}}^2} \\ I_{2\mathrm{c}} &= \frac{2\sqrt{2}U_{\mathrm{d}}\omega_{\mathrm{c}}^2C_{\mathrm{f2}}^2k\sqrt{L_1L_2}}{\pi L_{\mathrm{f1}}}\cos\frac{\theta}{2}\sqrt{R'^2_{\mathrm{L}}+Z_{\mathrm{f2}}^2} \\ I_{\mathrm{in-c}} &= \frac{2\sqrt{2}U_{\mathrm{d}}}{\pi\omega_{\mathrm{c}}L_{\mathrm{f1}}}\cos\frac{\theta}{2}\sqrt{A_{\mathrm{inc}}^2+B_{\mathrm{inc}}^2} \end{aligned} \quad (53)$$

where $A_{1\mathrm{c}}$, $B_{1\mathrm{c}}$, $A_{\mathrm{inc}}$, and $B_{\mathrm{inc}}$ are written as

$$\begin{aligned} A_{1\mathrm{c}} &= Z_2\omega_{\mathrm{c}}^2C_{\mathrm{f2}}^2R'_{\mathrm{L}}B_{1\mathrm{c}} = Z_2\omega_{\mathrm{c}}^2C_{\mathrm{f2}}^2Z_{\mathrm{f2}}-1 \\ A_{\mathrm{inc}} &= \frac{k^2L_1L_2C_{\mathrm{f2}}^2R'_{\mathrm{L}}}{\omega_{\mathrm{c}}L_{\mathrm{f1}}^2C_{\mathrm{f1}}}B_{\mathrm{inc}} = \omega_{\mathrm{c}}^2C_{\mathrm{f1}}a_{\mathrm{c}}+1. \end{aligned} \quad (54)$$

From (53), with the coupling coefficient increasing, the RMS current $I_{2\mathrm{c}}$ and $I_{\mathrm{in\text{-}c}}$ also increase, whereas the RMS current $I_{1\mathrm{c}}$ maintain constant. In addition, the RMS current $I_{1\mathrm{c}}$, $I_{2\mathrm{c}}$, and $I_{\mathrm{in\text{-}c}}$ increase as the load.

Likewise, based on (28), (31), and (48), the RMS current in the CV mode can be expressed as

$$\begin{aligned} I_{1\mathrm{v}} &= \frac{2\sqrt{2}U_{\mathrm{d}}C_{\mathrm{f11}}}{\pi R'_{\mathrm{L}}}\cos\frac{\theta}{2}\sqrt{A_{1\mathrm{v}}^2+B_{1\mathrm{v}}^2} \\ I_{2\mathrm{v}} &= \frac{2\sqrt{2}U_{\mathrm{d}}}{\pi\omega_{\mathrm{v}}L_{\mathrm{f1}}}\cos\frac{\theta}{2}\sqrt{A_{2\mathrm{v}}^2+B_{2\mathrm{v}}^2} \\ I_{3\mathrm{v}} &= \frac{2\sqrt{2}U_{\mathrm{d}}C_{\mathrm{f11}}}{\pi\omega_{\mathrm{v}}k\sqrt{L_1L_2}C_{\mathrm{f12}}R'_{\mathrm{L}}}\cos\frac{\theta}{2}\sqrt{Z_{\mathrm{f2}}^2+R'^2_{\mathrm{L}}} \\ I_{\mathrm{in-v}} &= \frac{2\sqrt{2}U_{\mathrm{d}}}{\pi\omega_{\mathrm{v}}L_{\mathrm{f1}}}\cos\frac{\theta}{2}\sqrt{A_{\mathrm{inv}}^2+B_{\mathrm{inv}}^2} \end{aligned} \quad (55)$$

where $A_{1\mathrm{v}}$, $B_{1\mathrm{v}}$, $A_{2\mathrm{v}}$, $B_{2\mathrm{v}}$, $A_{\mathrm{inv}}$, and $B_{\mathrm{inv}}$ are written as

$$\begin{aligned} A_{1\mathrm{v}} &= Z_{\mathrm{f2}}\left(1-\frac{Z_{1-\mathrm{v}}Z_2}{\omega_{\mathrm{v}}^2k^2L_1L_2}\right) \\ B_{1\mathrm{v}} &= Z_{1-\mathrm{v}}\left(\frac{Z_2R'_{\mathrm{L}}}{\omega_{\mathrm{v}}^2k^2L_1L_2}+\frac{L_{\mathrm{f2}}^2}{k^2L_1L_2}\right) \\ A_{2\mathrm{v}} &= \frac{Z_2Z_{\mathrm{f2}}C_{\mathrm{f2}}-L_{\mathrm{f2}}}{\omega_{\mathrm{v}}^3k^2L_1L_2C_{\mathrm{f12}}C_{\mathrm{f2}}R'_{\mathrm{L}}}B_{2\mathrm{v}} = \frac{Z_2}{\omega_{\mathrm{v}}^3k^2L_1L_2C_{\mathrm{f12}}} \\ A_{\mathrm{inv}} &= \frac{\omega_{\mathrm{v}}L_{\mathrm{f2}}^3C_{\mathrm{f11}}C_{\mathrm{f2}}}{C_{\mathrm{f12}}^2k^2L_1L_2R'_{\mathrm{L}}}B_{\mathrm{inv}} = \frac{C_{\mathrm{f11}}a_{\mathrm{v}}}{\omega_{\mathrm{v}}^3C_{\mathrm{f12}}^2k^2L_1L_2}+1. \end{aligned} \quad (56)$$

From (55), either as the coupling coefficient rises or as the load rises, the RMS current $I_{1\mathrm{v}}$, $I_{2\mathrm{v}}$, $I_{3\mathrm{v}}$, and $I_{\mathrm{in\text{-}v}}$ decrease in the CV mode.

The voltage stress of the resonant capacitors is an integral part of the proposed IPT system design. Therefore, it is necessary to analyze the voltage of the resonant capacitors in two modes.

Based on (11), (28), (53), and (55), the voltage of $C_1$, $C_2$, $C_{\mathrm{f1}}$, and $C_{\mathrm{f2}}$ in the CC mode and CV mode can be deduced as

$$\begin{aligned} U_{\mathrm{Cf1-c}} &= \frac{2\sqrt{2}U_{\mathrm{d}}}{\pi\omega_{\mathrm{c}}^2L_{\mathrm{f1}}C_{\mathrm{f1}}}\cos\frac{\theta}{2}\sqrt{\left(A_{\mathrm{inc}}-A_{1\mathrm{c}}\right)^2+\left(B_{\mathrm{inc}}-B_{1\mathrm{c}}\right)^2} \\ U_{\mathrm{C1-c}} &= \frac{2\sqrt{2}U_{\mathrm{d}}}{\pi\omega_{\mathrm{c}}^2L_{\mathrm{f1}}C_1}\cos\frac{\theta}{2}\sqrt{A_{1\mathrm{c}}^2+B_{1\mathrm{c}}^2} \\ U_{\mathrm{Cf2-c}} &= \frac{2\sqrt{2}U_{\mathrm{d}}\omega_{\mathrm{c}}k\sqrt{L_1L_2}}{\pi}\cos\frac{\theta}{2}\sqrt{\left(\frac{C_{\mathrm{f2}}R'_{\mathrm{L}}}{L_{\mathrm{f1}}}\right)^2+\left(\frac{C_{\mathrm{f2}}Z_{\mathrm{f2}}}{L_{\mathrm{f1}}}-C_{\mathrm{f1}}\right)^2} \\ U_{\mathrm{C2-c}} &= \frac{2\sqrt{2}U_{\mathrm{d}}\omega_{\mathrm{c}}C_{\mathrm{f2}}^2k\sqrt{L_1L_2}}{\pi L_{\mathrm{f1}}C_2}\cos\frac{\theta}{2}\sqrt{R'^2_{\mathrm{L}}+Z_{\mathrm{f2}}^2} \\ U_{\mathrm{Cf1-v}} &= \frac{2\sqrt{2}U_{\mathrm{d}}}{\pi\omega_{\mathrm{v}}^2L_{\mathrm{f1}}C_{\mathrm{f1}}}\cos\frac{\theta}{2}\sqrt{\left(A_{\mathrm{inv}}-A_{2\mathrm{v}}\right)^2+\left(B_{\mathrm{inv}}-B_{2\mathrm{v}}\right)^2} \\ U_{\mathrm{C1-v}} &= \frac{2\sqrt{2}U_{\mathrm{d}}}{\pi\omega_{\mathrm{v}}^2L_{\mathrm{f1}}C_1}\cos\frac{\theta}{2}\sqrt{A_{2\mathrm{v}}^2+B_{2\mathrm{v}}^2} \\ U_{\mathrm{Cf2-v}} & \end{aligned} \quad (57)$$

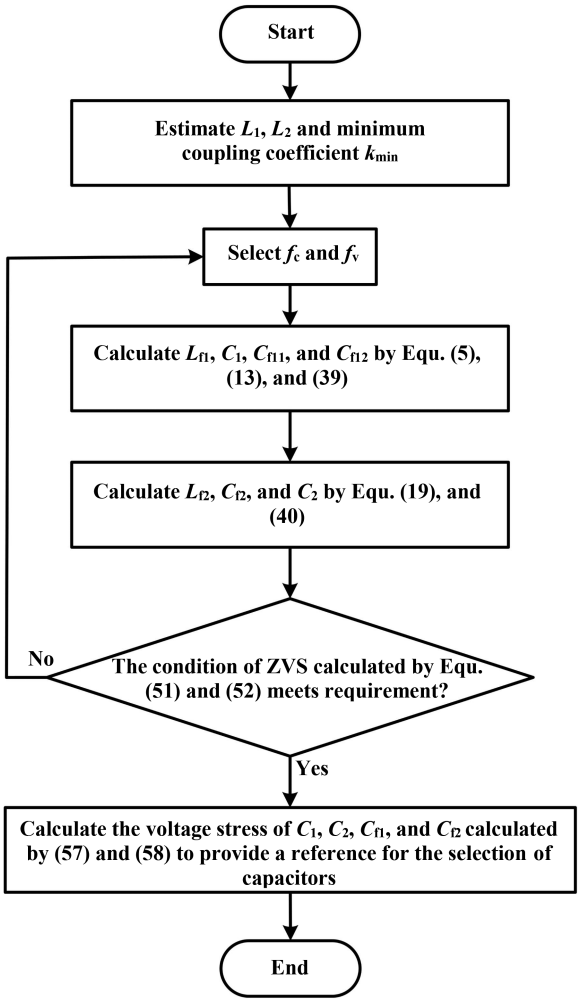


Fig. 5. Design procedure of the proposed LCC–LCC IPT converter.

$$= \frac{2\sqrt{2}U_{\mathrm{d}}C_{\mathrm{f11}}}{\pi\omega_{\mathrm{v}}k\sqrt{L_1L_2}C_{\mathrm{f12}}C_{\mathrm{f2}}R'_{\mathrm{L}}}\cos\frac{\theta}{2}\sqrt{\left(\frac{1+Z_{\mathrm{f2}}C_{\mathrm{f2}}}{C_{\mathrm{f2}}R'_{\mathrm{L}}}\right)^2+1}$$

$$U_{\mathrm{C2-v}} = \frac{2\sqrt{2}U_{\mathrm{d}}C_{\mathrm{f11}}}{\pi\omega_{\mathrm{v}}^2k\sqrt{L_1L_2}C_{\mathrm{f12}}C_2R'_{\mathrm{L}}}\cos\frac{\theta}{2}\sqrt{Z_{\mathrm{f2}}^2+R'^2_{\mathrm{L}}}. \quad (58)$$

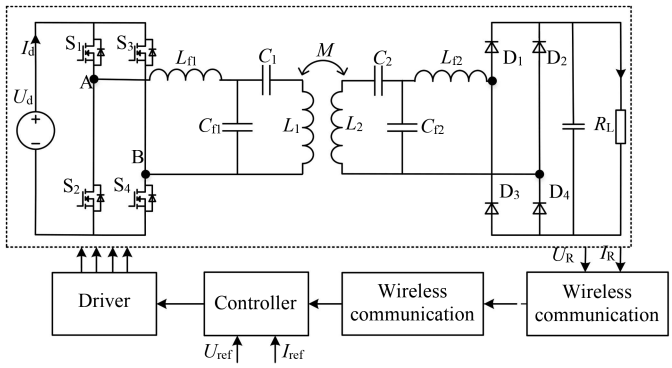


Fig. 6. Schematic diagram of the proposed IPT system.

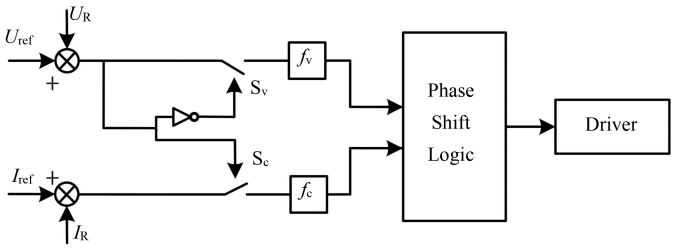


Fig. 7. Schematic of control logic for the IPT charger.

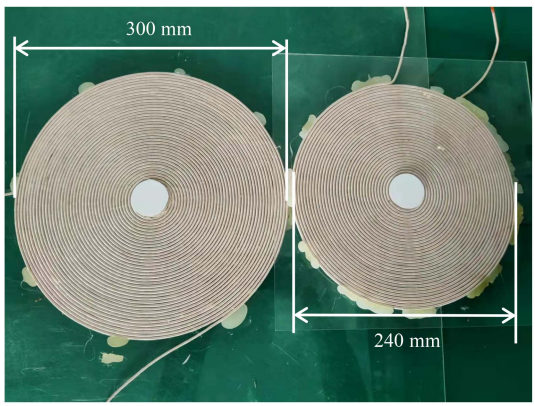


Fig. 8. Experimental platform for LCC–LCC IPT converter.

## III. Design of the LCC–LCC IPT Converter With the Proposed Method

### A. Parametric Design Procedure of the Presented Method

As analyzed in the previous section, the load-independent and misalignment-tolerant characteristics of the proposed converter are deduced for implementing two output modes. However, in the practical design process, a set of parameters are required to achieve two characteristics. Consequently, the practical design procedure is illustrated in Fig. 5 and as follows.

*Step 1:* The self-inductance of coils at the transmitting and receiving sides need to be estimated by considering the volume of the practical system. In addition, the minimum coupling coefficient $k_{\min}$ should be determined based on air gap and maximum misalignment between two coils to ensure the operating system in the inductive region.

*Step 2:* The resonant frequencies at two output modes should be selected for designing the parameter of compensation topology. For the IPT system, the lower frequency will result in larger compensation elements and the higher frequency will increase the complexity of the system design. Therefore, the operating frequency of IPT systems is selected between 20 and 95 kHz [24], [25], [26], [27], [28], [29], [30], [31]. Thus, the resonant frequencies of CC mode and CV mode can be selected as 81 and 90 kHz, respectively.

*Step 3:* Assuming $k = k_{\min}$, $a_{\mathrm{c}} = 0$, and $a_{\mathrm{v}} = 0$, the value for $L_{\mathrm{f1}}$, $C_{\mathrm{f11}}$, $C_{\mathrm{f12}}$, and $C_1$ can be calculated by using (5), (13), and (39). Furthermore, $C_{\mathrm{f2}}$, $C_2$, and $L_{\mathrm{f2}}$ can be determined from (19) and (40).

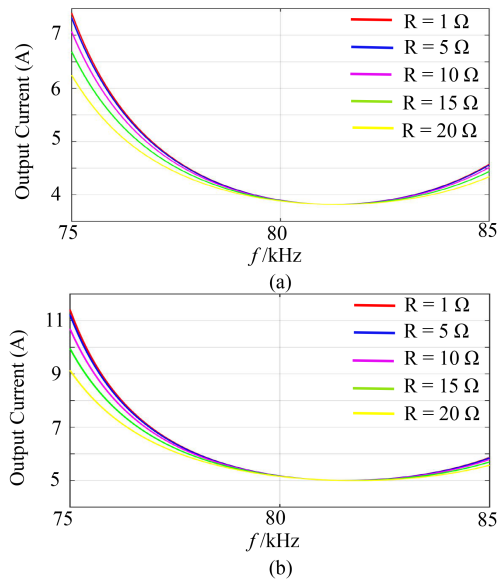


Fig. 9. Output current of the LCC–LCC compensation topology for various load under different coupling coefficient. (a) $k = 0.23$. (b) $k = 0.3$.

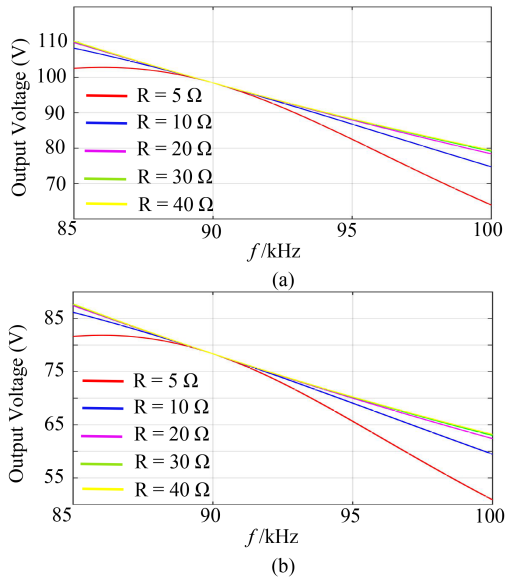


Fig. 10. Output voltage of the LCC–LCC compensation topology for various load under different coupling coefficient. (a) $k = 0.23$. (b) $k = 0.3$.

*Step 4:* It is indispensable to check whether the condition of ZVS calculated by (51) and (52) is satisfied during the entire charging process. If the results are not satisfied, the resonant frequencies need to be reselected.

*Step 5:* The voltage stress of $C_1$, $C_2$, $C_{f1}$, and $C_{f2}$ in two modes can be calculated by (57) and (58) to provide a reference for the selection of capacitors.

### B. Design of the Controller

Once parameters of compensation components are determined according to the above procedure, the system operates at different resonant frequencies for achieving CC output and CV output. However, variations of the coupling coefficient will change the output current and output voltage of the system at resonant frequencies. Therefore, the controller is required to maintain constant current and constant voltage in the actual situation. The schematic diagram of the proposed IPT system is presented in Fig. 6. The load voltage $U_R$ and load current $I_R$ are sampled and transmitted to the controller as feedback signals. Then, feedback signals are transmitted to the controller to enable the driver module to generate switching signals.

The control logic of the controller is shown in Fig. 7. The first step is to compare the load voltage with the reference value to determine whether the system should be operated in CC mode, i.e., $S_v = 0$ and $S_c = 1$, or CV mode, i.e., $S_v = 1$ and $S_c = 0$. Then, the switching logic of MOSFETs generated by the conventional phase shift control is transmitted to the driver module.

TABLE I
PARAMETER OF THE PRIMARY AND SECONDARY COILS

| Parameter | value |
|---|---|
| Lize wire (strand diameter, N. of strand) | 0.1 mm, 500 |
| Diameter and turns number of the primary winding | 240 mm*240 mm, 32 |
| Diameter and turns number of the secondary winding | 300 mm*300 mm, 41 |
| Air Gap | 75 mm - 110 mm |
| Self-inductance of primary $L_1$ | 208 $\mu$H |
| Self-inductance of secondary $L_2$ | 128 $\mu$H |
| Coupling coefficient | 0.23-0.3 |

TABLE II
COMPENSATION NETWORK PARAMETERS

| Symbols | Parameters | Value |
|---|---|---|
| $L_{f1}$ | Primary Compensation Inductor | 13μH |
| $C_{f1}$ | Primary Parallel Capacitor | 305nF |
| $C_1$ | Primary Series Capacitor | 19nF |
| $L_{f2}$ | Secondary Compensation Inductor | 31μH |
| $C_{f2}$ | Secondary Parallel Capacitor | 101nF |
| $C_2$ | Secondary Series Capacitor | 46nF |
| $f_c$ | Operating Frequency in CC Mode | 81kHz |
| $f_v$ | Operating Frequency in CV Mode | 90kHz |

## IV. RESULTS AND DISCUSSION OF SIMULATION AND EXPERIMENT

Since the misalignment tolerance of the compensation network is investigated in this article, the conventional circular coil is adopted. Fig. 8 shows two coils at the transmitting and receiving sides and the parameters of the coils are shown in Table I. The parameters of compensation components can be determined assuming $k_{min} = 0.2$ for operating the system in the inductive region as depicted in Table II.

### A. Simulation Validation

Based on Tables I and II, the output current as the function of the operating frequency with different equivalent ac loads is shown in Fig. 9 under different coupling coefficients. There are two conclusions that can be drawn from Fig. 9(a) and (b). On the one hand, at a constant coupling coefficient, if the operating frequency $f_c$ is 81 kHz, the output current is independent of the load. On the other hand, when the coupling coefficient varies, the

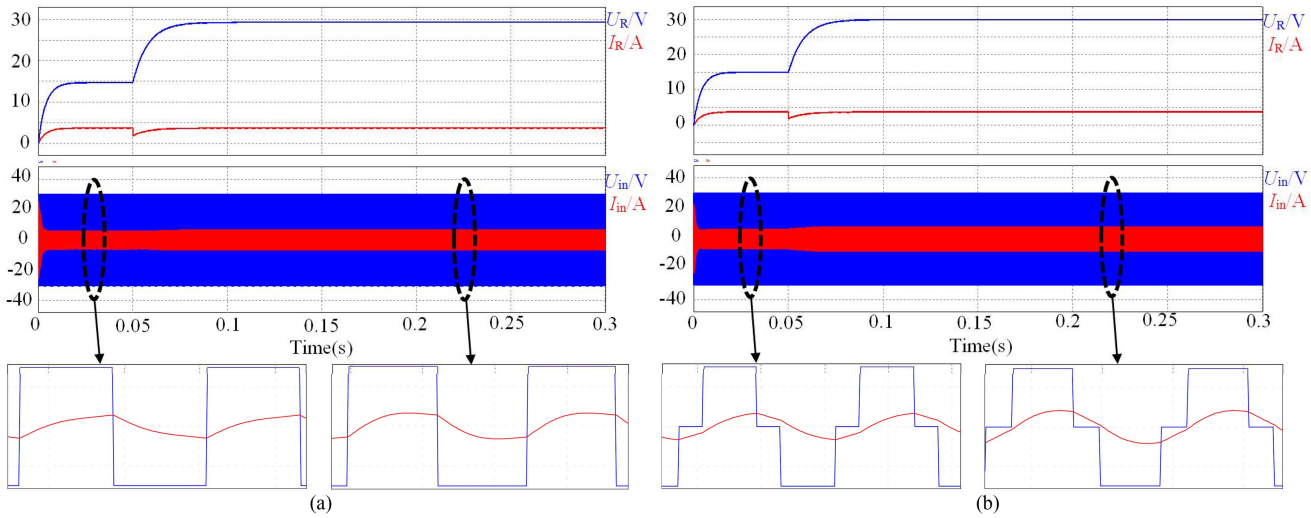


Fig. 11. Simulations of the LCC–LCC compensation topology in the CC mode. (a) $k = 0.23$. (b) $k = 0.3$.

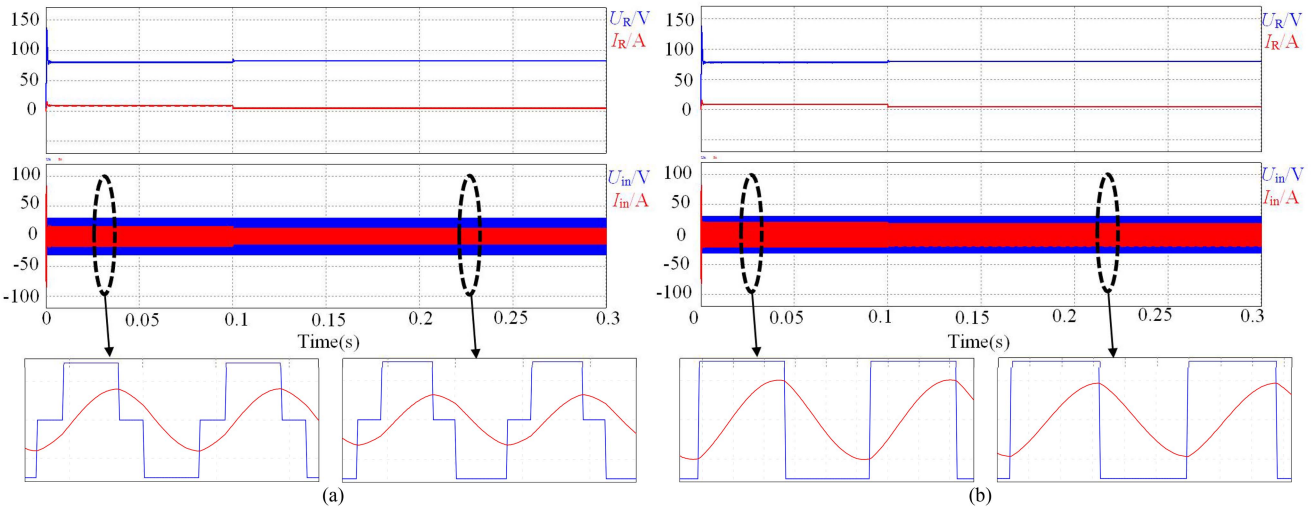


Fig. 12. Simulations of the LCC–LCC compensation topology in the CV mode. (a) $k = 0.23$. (b) $k = 0.3$.

resonant frequency is constant and remains 81 kHz, whereas the output current at $f_c = 81$ kHz increases with increasing coupling coefficient. In addition, when the resonant frequency varies by 3%, i.e., the range of the frequency is from 78 to 84 kHz, the maximum variation of the output current is 8.7% but can be modified by adjusting the phase shift angle.

The output voltage as the function of the operating frequency with different equivalent ac loads is shown in Fig. 10 under different coupling coefficients. Several similar conclusions can be drawn from Fig. 10 that the load-independent characteristic of the output voltage is implemented at the operating frequency $f_v$ (90 kHz), and the resonant frequency maintains constant and is unaffected by the coupling coefficient. Similarly, when the resonant frequency varies by 3%, i.e., the range of the frequency is from 87 to 93 kHz, the maximum variation of the output voltage is 7.7% but can be modified by adjusting the phase shift angle.

As a result, with the proposed design method, the effects of variations in the coupling coefficient and load are effectively minimized. The proposed IPT converter can operate at a constant frequency whether in the CC mode or CV mode.

Fig. 11 shows simulations of the LCC–LCC converter in the CC mode. In Fig. 11(a), when the output power varies from 120 to 60 W, the output current with a 0.75% variation remains 3.7 A at $k = 0.23$. Comparing Fig. 11(a) to (b), when $k$ is from 0.23 to 0.3, the output current maintains 3.7 A by adjusting the phase shift angle $\theta$ from 0° to 49° and at $k = 0.3$, the frequency, at which the load-independent CC output characteristic is also implemented, remains 81 kHz. In addition, in the CC mode, whether $k = 0.23$ or $k = 0.3$, ZVS can be achieved under different output power.

Fig. 12 shows simulations of the LCC–LCC converter in the CV mode. Several similar conclusions can be deduced from Fig. 12. On the one hand, at the constant coupling coefficient,

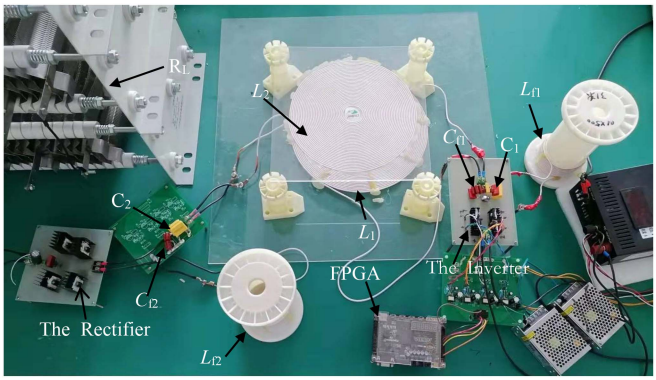


Fig. 13. Experimental platform for LCC–LCC IPT converter.

the output voltage maintains at 78 V during different output power and the maximum variation is 1.2%. On the other hand, when $k$ is varied from 0.23 to 0.3, the output current maintains a constant value at 78 V by adjusting the phase shift angle $\theta$ from 51° to 0°. Furthermore, in the CV mode, whether $k = 0.23$ or $k = 0.3$, the operating frequency maintains 90 kHz and ZVS is also implemented.

### B. Experimental Validation

As is shown in Fig. 13, to verify the effectiveness and practicability of the presented method, a prototype of 120 W using LCC–LCC IPT converter has been constructed. Here, four MOSFETs with manufacturer part number SPW47N60C3 make up the primary dc–ac full-bridge inverter, and four fast-recovery diodes (MUR860T) consist of the secondary rectifier. An ALTBRA EPCE10F17C8N FPGA is adopted as the closed-loop controller. In this article, we focus on a novel design method to implement the load-independent and misalignment-tolerant characteristics of the LCC–LCC compensation topology for charging energy storage load. Thus, the wireless feedback circuit should be replaced by wired communication. Since the charging cycle of energy storage devices is generally long, the load is replaced with a variable resistance in this article.

Figs. 14 and 15 illustrate actual waveforms of the presented LCC–LCC IPT converter in the CC mode under various output power. As shown in Fig. 13(a) and (b), at $k = 0.23$, changing the output power from 100% to 50%, the load current $I_{\mathrm{R}}$ keeps constant at 3.6 A and the variation of that is merely 2.4% when the phase shift angle $\theta$ maintains a constant value and equals 0. Also, at $k = 0.3$, the same conclusion can be obtained from Fig. 14(a) and (b). This means that regardless of the coupling coefficient, the load-independent output current is implemented at 81 kHz. Besides, several conclusions can be deduced by comparing Fig. 13(a) with Fig. 14(a). On the one hand, the output current, whose variation is merely 1.3%, remains 3.6 A by adjusting the phase shift angle from 0° to 43°, when the coupling coefficient $k = 0.23$ and $k = 0.3$. On the other hand, the operating frequency $f_{\mathrm{c}}$ (81 kHz) maintains a constant value unaffected by the coupling coefficient. ZVS can also be implemented over different output power and coupling coefficients in the CC mode.

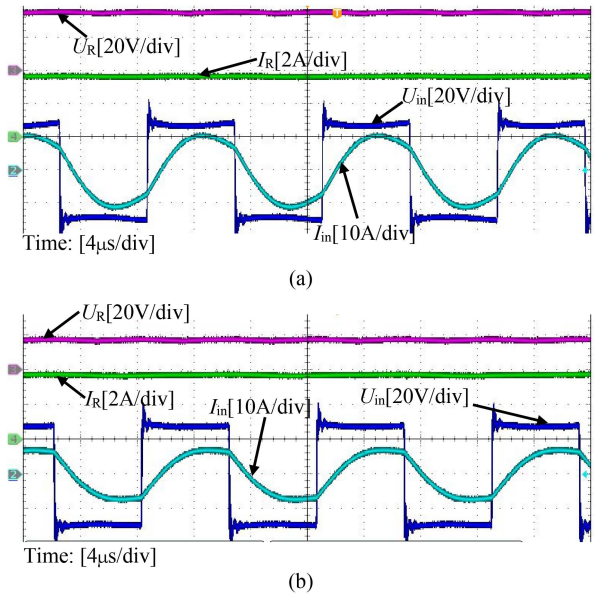


Fig. 14. Experimental waveforms of the output current, output voltage, input current and input voltage in the CC mode with different output power under $k = 0.23$. (a) Rated power. (b) 50% of rated power.

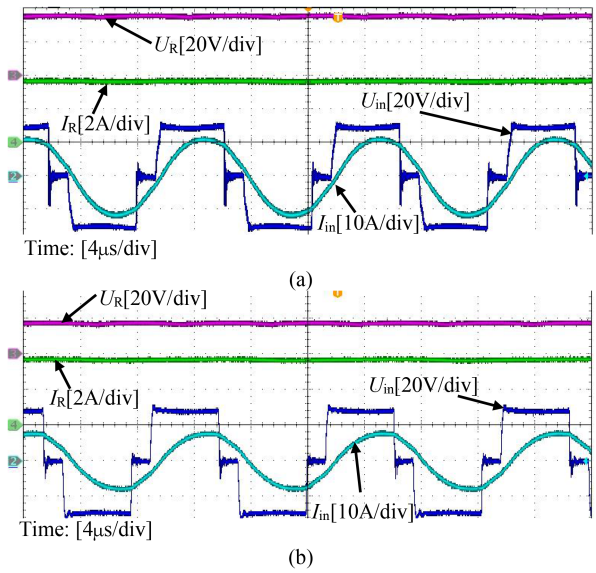


Fig. 15. Experimental waveforms of the output current, output voltage, input current, and input voltage in the CC mode with different output power under $k = 0.3$. (a) Rated power. (b) 50% of rated power.

In the CC mode, there are two small errors in the experimental results compared to the simulation. First, the output current is reduced by 0.1 A, as a result of the equivalent series resistances of compensation elements. Second, the maximum phase shift angle is reduced by 6° due to the measurement tolerance in the coupling coefficient.

Actual waveforms of the presented LCC–LCC IPT converter in the CV mode under various output power are illustrated in Figs. 16 and 17. It is concluded from Fig. 16(a) and (b) that at $k = 0.3$, the load voltage $U_{\mathrm{R}}$ maintains nearly constant at 77 V, i.e., the variation is only 1.0%, when the output power is altered

TABLE III
COMPARISON OF DIFFERENT DESIGN METHODS FOR THE LCC–LCC COMPENSATION TOPOLOGY WITH THE PROPOSED METHOD

| Design Method | No. of additional C | No. of additional L | No. of additional switches | Load-independent output voltage | Load-independent output current | $k$-independent resonant frequency | $k$-independent output voltage | $k$-independent output current |
|---|---|---|---|---|---|---|---|---|
| Proposed | 0 | 0 | 0 | Yes | Yes | Yes | Yes | Yes |
| [24] | 40 | 0 | 40 | No | Yes | Yes | No | Yes |
| [25] | 1 | 0 | 0 | No | Yes | Yes | No | Yes |
| [26] | 0 | 1 | 2 | Yes | Yes | Yes | No | No |
| [27] | 0 | 1 | 2 | Yes | Yes | Yes | No | No |
| [28] | 0 | 0 | 0 | Yes | Yes | No | No | No |
| [29] | 0 | 0 | 0 | Yes | Yes | No | No | No |
| [30] | 0 | 0 | 0 | Yes | Yes | No | No | No |
| [31] | 0 | 0 | 0 | Yes | Yes | No | No | No |

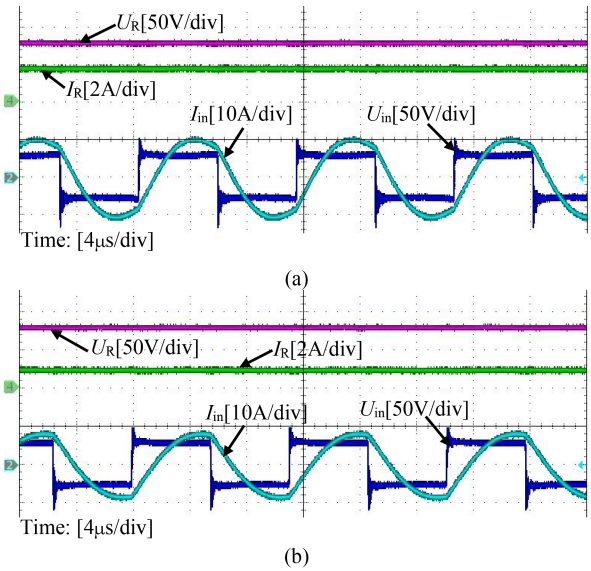


Fig. 16. Experimental waveforms of the output current, output voltage, input current, and input voltage in the CV mode with different output power under $k = 0.3$. (a) Rated power. (b) 50% of rated power.

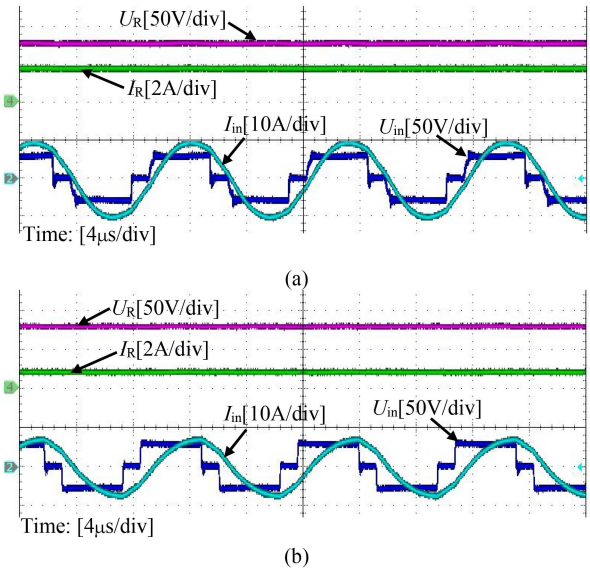


Fig. 17. Experimental waveforms of the output current, output voltage, input current, and input voltage in the CV mode with different output power under $k = 0.23$. (a) Rated power. (b) 50% of rated power.

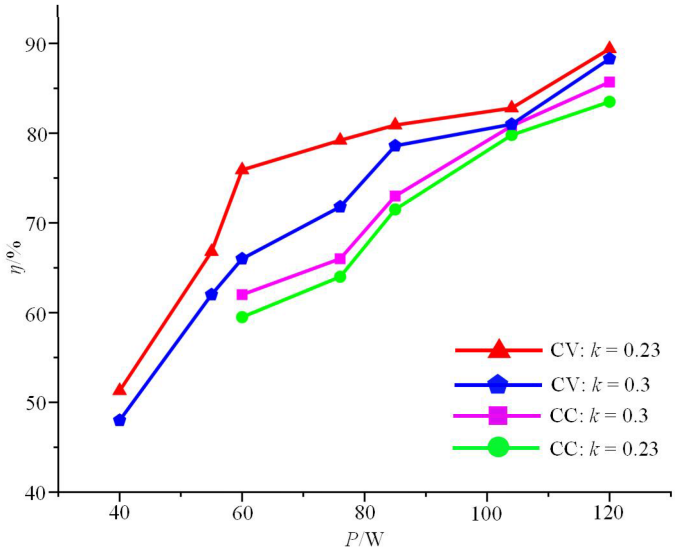


Fig. 18. DC–DC efficiency at different misalignment and output power.

from 100% to 50%. Furthermore, based on Fig. 17(a) and (b), $U_R$ also keeps nearly constant under different output power when the phase shift angle keeps 46° at $k = 0.23$. Comparing Fig. 16(a) with Fig. 17(a), some conclusions can be derived. When the coupling coefficient $k = 0.3$, the output voltage remains the same as that at $k = 0.23$ by adjusting the phase shift angle $\theta$ from 0° to 46°. Moreover, it can be found that the operating frequency remains 90 kHz, no matter what the coupling coefficient. ZVS can also be implemented over different output power and coupling coefficients in the CV mode.

In the CV mode, in contrast to simulation, several minor errors exist in the experimental results. On the one hand, the maximum reduction of the output voltage is 1.2%, since there are equivalent series resistances of compensation elements. On the other hand, the maximum phase shift angle is reduced by 5° owing to the measurement tolerance in the coupling coefficient.

Fig. 18 shows the dc–dc efficiency of the converter at different coupling coefficients and output power. It can be noticed that regardless of the coupling coefficient, the efficiency increases as the output power in the two output modes. At the rated power, the peak efficiency in the CC mode is 85.7% under $k = 0.3$, whereas the peak efficiency in the CV mode is 89.4% under $k = 0.23$. Owing to the increase of reactive power caused by

variations of the coupling coefficient, the efficiency decreases at other coupling coefficients.

The comparison of other design methods for the LCC–LCC compensation topology with the proposed method is illustrated in Table III. It is deduced from [28], [29], [30], and [31] that without additional components, variations of the coupling coefficient $k$ affect the resonant frequency, the output voltage, and the output current. According to [24], [25], [26], and [27], owing to the application of additional compensation components, the complexity of the system is increased and the implementation of two output modes is limited. As a result, the most important benefit of the proposed method is that the resonant frequency in two output modes maintains constant unaffected by the variation of the coupling coefficient $k$.

## V. Conclusion

In this article, a novel design method of the LCC–LCC compensation topology is proposed to implement CC/CV charging of the IPT systems. The LCC–LCC compensation network is precisely designed to achieve constant output current/voltage regardless of the load and coupling coefficient. In comparison to other parametric design methods, the most significant advantage is that the resonant frequency, at which the load-independent output characteristic is implemented, maintains constant whether in CC or CV mode. Consequently, the influence of the misalignment can be greatly diminished and both two output modes can be achieved with a single converter only by the conventional phase shift control strategy. The excellent behavior of the proposed system with respect to a stable operation has been validated by experimental results.

## References


[1] Z. Zhang, H. Pang, A. Georgiadis, and C. Cecati, "Wireless power transfer—An overview," *IEEE Trans. Ind. Electron.*, vol. 66, no. 2, pp. 1044–1058, Feb. 2019.

[2] B. Yang, Y. Chen, W. Ruan, H. Liu, Y. Ren, and R. Mai, "Current stress optimization for double-sided CLLLC topology-based IPT system with constant output current tolerating pad misalignments," *IEEE Trans. Ind. Electron.*, vol. 58, no. 1, pp. 1032–1043, Jan./Feb. 2022.

[3] Y. C. Liu, J. Zhang, C. K. Tse, C. Zhu, and S.-C. Wong, "General pathways to higher order compensation circuits for IPT converters via sensitivity analysis," *IEEE Trans. Power Electron.*, vol. 36, no. 9, pp. 9897–9906, Sep. 2021.

[4] S. Jeong, Y. J. Jang, D. Kum, and M. S. Lee, "Charging automation for electric vehicles: Is a smaller battery good for the wireless charging electric vehicles?," *IEEE Trans. Automat. Sci. Eng.*, vol. 16, no. 1, pp. 486–497, Jan. 2019.

[5] M. Schormans, V. Valente, and A. Demosthenous, "Practical inductive link design for biomedical wireless power transfer: A tutorial," *IEEE Trans. Biomed. Circuits Syst.*, vol. 12, no. 5, pp. 1112–1130, Oct. 2018.

[6] D. Patil, M. K. McDonough, J. M. Miller, B. Fahimi, and P. T. Balsara, "Wireless power transfer for vehicular applications: Overview and challenges," *IEEE Trans. Transp. Electrific.*, vol. 4, no. 1, pp. 3–37, Mar. 2018.

[7] T. Lee, S. Huang, S. Dai, and J. Su, "Design of misalignment-insensitive inductive power transfer via interoperable coil module and dynamic power control," *IEEE Trans. Power Electron.*, vol. 35, no. 9, pp. 9024–9033, Sep. 2020.

[8] G. R. Nagendra, G. A. Covic, and J. T. Boys, "Determining the physical size of inductive couplers for IPT EV systems," *IEEE J. Emerg. Sel. Topics Power Electron.*, vol. 2, no. 3, pp. 571–583, Sep. 2014.

[9] F. Lu, H. Zhang, H. Hofmann, W. Su, and C. C. Mi, "A dual-coupled LCC-compensated IPT system with a compact magnetic coupler," *IEEE Trans. Power Electron.*, vol. 33, no. 7, pp. 6391–6402, Jul. 2018.

[10] I. Cortes and W. Kim, "Lateral position error reduction using misalignment-sensing coils in inductive power transfer systems," *IEEE ASME Trans. Mechatronics*, vol. 23, no. 2, pp. 875–882, Apr. 2018.

[11] X. Zhang, F. Liu, and T. Mei, "Multifrequency phase-shifted control for multiphase multiload MCR WPT system to achieve targeted power distribution and high misalignment tolerance," *IEEE Trans. Power Electron.*, vol. 36, no. 1, pp. 991–1003, Jan. 2021.

[12] L. Zhao, D. J. Thrimawithana, U. K. Madawala, A. P. Hu, and C. C. Mi, "A misalignment-tolerant series-hybrid wireless EV charging system with integrated magnetics," *IEEE Trans. Power Electron.*, vol. 34, no. 2, pp. 1276–1285, Feb. 2019.

[13] B. Luo, T. Long, L. Guo, R. Dai, R. Mai, and Z. He, "Analysis and design of inductive and capacitive hybrid wireless power transfer system for railway application," *IEEE Trans. Ind. Appl.*, vol. 56, no. 3, pp. 3034–3042, May/Jun. 2020.

[14] F. Lu, H. Zhang, H. Hofmann, and C. C. Mi, "An inductive and capacitive combined wireless power transfer system with LC-compensated topology," *IEEE Trans. Power Electron.*, vol. 31, no. 12, pp. 8471–8482, Dec. 2016.

[15] Y. Chen, R. Mai, Y. Zhang, M. Li, and Z. He, "Improving misalignment tolerance for IPT system using a third-coil," *IEEE Trans. Power Electron.*, vol. 34, no. 4, pp. 3009–3013, Apr. 2019, doi: 10.1109/TPEL.2018.2867919.

[16] X. Qu, Y. Yao, D. Wang, S. Wong, and C. K. Tse, "A family of hybrid IPT topologies with near load-independent output and high tolerance to pad misalignment," *IEEE Trans. Power Electron.*, vol. 35, no. 7, pp. 6867–6877, Jul. 2020.

[17] C. S. Wong, Y. P. Chan, L. Cao, L. Wang, K. H. Loo, and M. C. Wong, "A single-stage dynamically compensated IPT converter with unity power factor and constant output voltage under varying coupling condition," *IEEE Trans. Power Electron.*, vol. 35, no. 10, pp. 10121–10136, Oct. 2020.

[18] J. Mai, Y. Wang, Y. Yao, and D. Xu, "Analysis and design of high-misalignment-tolerant compensation topologies with constant-current or constant-voltage output for IPT systems," *IEEE Trans. Power Electron.*, vol. 36, no. 3, pp. 2685–2695, Mar. 2021.

[19] Y. Wang, J. Mai, Y. Yao, and D. Xu, "Analysis and design of an IPT system based on S/SP compensation with improved output voltage regulation," *IEEE Trans. Ind. Inform.*, vol. 16, no. 5, pp. 3256–3266, May 2020.

[20] B. Yang et al., "Analysis and design of a T/S compensated IPT system for AGV maintaining stable output current versus air gap and load variations," *IEEE Trans. Power Electron.*, vol. 37, no. 5, pp. 6217–6228, May 2022.

[21] Z. Zhang, F. Zhu, D. Xu, P. T. Krein, and H. Ma, "An integrated inductive power transfer system design with a variable inductor for misalignment tolerance and battery charging applications," *IEEE Trans. Power Electron.*, vol. 35, no. 11, pp. 11544–11556, Nov. 2020.

[22] H. Zhang, Y. Chen, C.-H. Jo, S.-J. Park, and D.-H. Kim, "DC-link and switched capacitor control for varying coupling conditions in inductive power transfer system for unmanned aerial vehicles," *IEEE Trans. Power Electron.*, vol. 36, no. 5, pp. 5108–5120, May 2021.

[23] D. Wang, X. Qu, Y. Yao, and P. Yang, "Hybrid inductive-power-transfer battery chargers for electric vehicle onboard charging with configurable charging profile," *IEEE Trans. Intell. Transp. Syst.*, vol. 22, no. 1, pp. 592–599, Jan. 2021.

[24] K. Zhang, W. Gao, R. Shi, Z. Yan, B. Song, and A. P. Hu, "An impedance matching network tuning method for constant current output under mutual inductance and load variation of IPT system," *IEEE Trans. Power Electron.*, vol. 35, no. 10, pp. 11108–11118, Oct. 2020.

[25] Y. Chen, R. Mai, Y. Zhang, M. Li, and Z. He, "Improving misalignment tolerance for IPT system using a third-coil," *IEEE Trans. Power Electron.*, vol. 34, no. 4, pp. 3009–3013, Apr. 2019, doi: 10.1109/TPEL.2018.2867919.

[26] B. Cheng and L. He, "High-order network based general modeling method for improved transfer performance of the WPT system," *IEEE Trans. Power Electron.*, vol. 36, no. 11, pp. 12375–12388, Nov. 2021.

[27] D. Wang, X. Qu, Y. Yao, and P. Yang, "Hybrid inductive-power-transfer battery chargers for electric vehicle onboard charging with configurable charging profile," *IEEE Trans. Intell. Transp. Syst.*, vol. 22, no. 1, pp. 592–599, Jan. 2021.

[28] V. Vu, D. Tran, and W. Choi, "Implementation of the constant current and constant voltage charge of inductive power transfer systems with the double-sided LCC compensation topology for electric vehicle battery charge applications," *IEEE Trans. Power Electron.*, vol. 33, no. 9, pp. 7398–7410, Sep. 2018.

[29] J. Lu, G. Zhu, D. Lin, S. Wong, and J. Jiang, "Load-Independent voltage and current transfer characteristics of high-order resonant network in IPT system," *IEEE J. Emerg. Sel. Topics Power Electron.*, vol. 7, no. 1, pp. 422–436, Mar. 2019.
[30] X. Qu, H. Chu, S. Wong, and C. K. Tse, "An IPT battery charger with near unity power factor and load-independent constant output combating design constraints of input voltage and transformer parameters," *IEEE Trans. Power Electron.*, vol. 34, no. 8, pp. 7719–7727, Aug. 2019.
[31] J. Lu, G. Zhu, D. Lin, Y. Zhang, J. Jiang, and C. C. Mi, "Unified load-independent ZPA analysis and design in CC and CV modes of higher order resonant circuits for WPT systems," *IEEE Trans. Transp. Electrific.*, vol. 5, no. 4, pp. 977–987, Dec. 2019.
[32] J. Min and M. Ordonez, "Unified bidirectional resonant frequency tracking for CLLC converters," *IEEE Trans. Power Electron.*, vol. 37, no. 5, pp. 5637–5649, May 2022.
[33] J. Min and M. Ordonez, "Bidirectional resonant frequency tracking for CLLC converters based on voltage falling edges," in *Proc. IEEE Energy Convers. Congr. Expo.*, pp. 1793–1797, Oct. 2021.
[34] X. Wang, J. Xu, M. Leng, H. Ma, and S. He, "A hybrid control strategy of LCC-S compensated WPT system for wide output voltage and ZVS range with minimized reactive current," *IEEE Trans. Ind. Electron.*, vol. 68, no. 9, pp. 7908–7920, Sep. 2021.

**Jingang Li** was born in Hebei Province, China, in 1968. He received the B.S. degree from Shaanxi Institute of Mechanics, Xi'an, China, in 1991, and the M.S. and Ph.D. degrees in electrical engineering from Xi'an University of Technology, Xi'an, China, in 1998 and 2007, respectively.

Since 1991, he has been with Xi'an University of Technology, where he has been an Associate Professor since 2003. His research interests mainly include high frequency, high efficiency power electronics converters, and control systems.

**Xuze Zhang** was born in Shaanxi Province, China, in 1994. He received the B.S. degree from Chang'an University, Xi'an, China, in 2016, and the M.S. degree in electrical engineering from Xi'an University of Technology, Xi'an, China, in 2020. He is currently working toward the Ph.D. degree with the School of Electrical Engineering.

His research interests mainly include wireless power transfer and high frequency resonant converters.

**Xiangqian Tong** (Member, IEEE) was born in Shaanxi, China, in 1961. He received the B.S. degree from Shaanxi Institute of Technology, Hanzhong, China, in 1983, the M.S. degree from the Xi'an University of Technology, Xi'an, China, in 1989, and the Ph.D. degree in electrical engineering from Xi'an Jiaotong University, Xi'an, China, in 2006.

In 1989, he was with Xi'an University of Technology, where he has been a Professor since 2002. His research interests include the application of power electronics in power systems and control of power quality.